This is a previous version of the article published in Advances in Space Research. 2018, 61(3): 862-878. doi:10.1016/j.asr.2017.10.054

Concurrent Image-based Visual Servoing with Adaptive Zooming for Non-cooperative Rendezvous Maneuvers

Jorge Pomares[1], Leonard Felicetti[2], Javier Pérez[3], and M. Reza Emami[4]

ABSTRACT

An image-based servo controller for the guidance of a spacecraft during non-cooperative rendezvous is presented in this paper. The controller directly utilizes the visual features from image frames of a target spacecraft for computing both attitude and orbital maneuvers concurrently. The utilization of adaptive optics, such as zooming cameras, is also addressed through developing an invariant-image servo controller. The controller allows for performing rendezvous maneuvers independently from the adjustments of the camera focal length, improving the performance and versatility of maneuvers. The stability of the proposed control scheme is proven analytically in the invariant space, and its viability is explored through numerical simulations.

Keywords: Non-Cooperative Rendezvous; Visual Servoing; Zooming Cameras, Spacecraft Guidance Navigation and Control.

1. Introduction

Space debris is becoming the issue of concern amongst the space community because of its repercussion on present and future space missions. Indeed, uncontrolled objects from the previous space missions are currently occupying important orbital slots, causing notable collision possibilities with operative and non-operative satellites [1]. Despite the recent adoption of some mitigation guidelines [3] and the development of a network of space debris surveillance and awareness [4][5], the threat of such incidents cannot be totally averted. Collisions, as the one between Iridium 33 and Cosmos 2251 in 2009 [6], are still probable, and they can trigger cascade phenomena that may compromise future utilization of space, labelled as Kessler

[1] Associate Professor, University of Alicante, POBox 99, 03080, Alicante, Spain. Email: jpomares@ua.es

[2] Associate Senior Lecturer, Luleå University of Technology, Division of Space Technology, Box 848, Rymdcampus, 981 28 Kiruna, Sweden. Email: leonard.felicetti@ltu.se

[3] Ph.D. Student, University of Alicante, POBox 99, 03080, Alicante, Spain. Email: javotron1@gmail.com

[4] Chair Professor, Onboard Space Systems, Luleå University of Technology, Division of Space Technology, Box 848, Rymdcampus, 981 28 Kiruna, Sweden. Email: reza.emami@ltu.se ; Space Mechatronics group, University of Toronto, Institute for Aerospace Studies, Toronto M3H 5T6, Canada; Email: reza.emami@utoronto.ca (corresponding author)

Syndrome [7][8][9]. Therefore, the need for a solution to this problem has led the space community to investigating the viability of different debris removal strategies [10] and the definition and development of on-orbit servicing missions for satellite rescuing and repairing [11]. Specifically, the removal of large, uncontrolled objects seems to be a viable solution for eliminating potential sources of new debris that could overcrowd low-Earth orbits. Further, on-orbit service missions have been thought for extending the operational life of satellites that cannot be easily removed by de-orbiting maneuvers but has to be dismissed in graveyard orbits at their end-of-life, mostly in Geostationary Earth orbits.

Preliminary analyses and design concepts of both debris removal and on-orbit servicing missions have shown that a close encounter to the debris by chasing spacecraft is a more promising approach than distance manipulations and "touchless" technologies, such electrostatic tug, laser ablation, etc. [10]. Regardless of the technology adopted for capturing the uncontrolled debris, e.g., robot manipulators, nets, harpoons etc., the rendezvous with an uncooperative objects can follow a well-defined scheme: The chaser spacecraft has to (a) reach the same orbit of the target debris; (b) perform phasing orbital maneuvers to reduce the distance from the target debris; (c) synchronize its attitude motion with respect to the target debris; and (d) perform the rendezvous maneuvers to allow for on-orbit servicing or debris grasping and removal operations [12].

An image-based approach is one of the most appealing choices for the uncooperative rendezvous, since this technique is considered a low cost, mainly passive and accurate [13]. Furthermore, the technology readiness of space qualified cameras, as well as of the onboard computers, is mature enough that the techniques developed for the control of ground based robots can be easily implemented onboard [14]. An example of automated rendezvous is the Automated Transfer Vehicle (ATV), where the relative position and attitude of the chasing vehicle with respect to the International Space Station (ISS) is reconstructed by identifying the visual features of a specific target attached to the ISS [15][16]. Another example is given by the PRISMA mission [17], where two different camera systems have been used during the formation flying demonstration experiment: the Far Range Camera and the Close Range Camera. The far range camera has been used as a star-tracker, detecting the target spacecraft as a bright spot over a diffuse black background. Thus, only information concerning the line of sight could be used in the guidance, navigation and control loop for reducing the distance down to 20-30m. The close range camera has been used instead for the proximity operations between the spacecraft, extracting more detailed visual features and reconstructing even the attitude of the target platform [18].

The previously mentioned missions demonstrated the viability of vision based GNC loops for the rendezvous of cooperative targets and the actual challenge is represented by the extension of such techniques to non-cooperative targets, such as space debris or satellites to be

recovered. The main difference between cooperative rendezvous and non-cooperative rendezvous is related to the target object that is generally not designed to perform a rendezvous. Therefore, the target does not send any information of its position to the chaser and it does not have specific "targets features" as well as specific docking system that can help the chaser spacecraft during the rendezvous and capture maneuvers. Further, the target satellite is generally tumbling, as the satellite is anymore able to control its attitude [19]. Therefore, the navigation system of the chaser satellite should address all the issues related to the target acquisition and target motion identification by means of specific onboard sensors and real time image processing algorithms. Moreover, the chaser should be able to obtain information concerning its accurate relative positioning even if, in general, the range is undetermined during the far-distance, angles-only, navigation phases [20]. Finally, the guidance system of the chaser should be designed in order to make possible the close approach to the target by taking into account the typology of the capture system as well as the characteristics and performance of the actuation system. In both [21] and [22], experimental setups have been settled in order to test the vision-based tracking algorithms to a space-like scenario. The experimental results showed the robustness of the classical algorithms to relative chaser/target orientation motions under different illumination conditions. In [23], the feasibility of a monocular-based relative navigation system, for rendezvous and docking of a fully unknown space object, has been investigated and successfully verified by using two extended Kalman filters applied to the far and close approach phases, respectively. The utilization of LIDARs as main sensors for close approaches to uncooperative objects has been explored in [24], [25] and [26]. Further, a combined algorithm which uses vision-based predictions and motion planning for the actuation of robotic arms during the pre and post grasping phases is presented in [27] and the application of visual servoing techniques to a dual arm robotic system is also investigated in [28]. Stereoscopic vision techniques can be also applied for close rendezvous, as in [29].

It is worth noting that the problem of vision based rendezvous has been always divided in far and close approach cases. This is essentially due to intrinsic characteristic of the used camera systems: optical system with fixed and predefined focal length have been implemented onboard in both ATV and PRISMA missions, as well as theoretical studies have been focused on the implementation of visual servoing techniques for close approaches to the target satellites. However, the use of adaptive optics, i.e. zooming cameras, could overcome these limitations and allow the development of an unified, robust and adaptive guidance and navigation strategy for the complete (far and close) rendezvous of uncooperative satellites. The current technology and the expected progresses on the development and integration of such kind of cameras onboard of space systems, allow the formulation and implementation of GNC schemes that use zooming cameras as main onboard sensing devices [30][31][32].

This paper proposes the use of a zooming camera to perform the guidance of a spacecraft with respect to an observed object using an image-based visual servoing approach. A review of the main visual servoing approaches is presented in [33] and [34], where two different categories of control are identified and named as "position-based" visual servoing and "image-based" visual servoing, respectively. The techniques applied to ATV and PRISMA missions, as an example, fall into the "position-based" visual servoing group. In fact, in these cases the image information is jointly used with known models of the observed objects for estimating the relative position and attitude of such objects with respect to the camera system. The "image-based" visual servoing system proposed in this paper, on the other hand, allows for defining a control law directly in the image domain. In this case, the system does not need any *a priori* knowledge of the 3D structure of the observed scene, thus being robust with respect to model uncertainties and disturbances. Only a set of visual features has to be extracted from the observed object and then tracked in the image plane during the maneuvers, allowing for a relative navigation without any estimation of both relative position and attitude of the target. Different methods can be used for extracting the visual features [35][36] and their space application has been verified by taking into account different simulated lighting conditions [22] and [37]. In this paper, it is assumed that all the image and pixels signal processing operations have been already performed by an image-processing unit, and a set of well-defined visual features in the image plane can be utilized by the controller to perform the desired maneuvers.

Further, the direct image-based visual servoing approaches existing in literature do not consider the orbital and attitude dynamics of the spacecraft as well as the real configuration of sensors and actuators, see e.g. [38][39][40]. In contrast, the inclusion of the spacecraft attitude and orbital dynamics in an image-based controller is addressed in this paper. The resulting control uses images from zooming cameras for concurrently controlling both the attitude and the orbital dynamics of the chaser spacecraft. Moreover, the developed visual servoing system adjusts the zoom of the camera for maintaining the selected visual features always within the field of view. For these reasons, a new direct image-based control has been developed in this paper through the definition of an error function using projective invariant properties. This error function is invariant to the changes with respect to the camera intrinsic parameters and is only dependent on the relative pose between the camera and target object. Therefore, the resulting controller allows for performing rendezvous maneuvers independently from the adjustments of the camera focal length, improving the performance and versatility of maneuvers.

The paper is divided into the following sections. Section 2 describes the system dynamics and the proposed image-based visual servoing system to perform the spacecraft guidance. Section 3 extends the previous visual servoing system for the control of a spacecraft using zooming cameras. The spacecraft behavior, during the tracking of different kind of trajectories

during the rendezvous phases, is described in Section 4 and the concluding remarks are presented in Section 5.

2. Non-Cooperative Rendezvous Modeling

The non-cooperative rendezvous involves a fully operative spacecraft, the chaser, and a non-controllable object, such as space debris to be removed or a damaged spacecraft to be recovered. To analyze the maneuvers, it is necessary to define coordinate frames which help the description and the definition of the system of equations of motion. In the following both the coordinate frames and the equations of motion are described.

2.1 Coordinate Frames

Figure 1 shows the coordinate frame attached to the body of the chasing spacecraft, named as {B}, and the coordinate frame associated to the object to be chased, named as target coordinate frame {T}. Both of them are orbiting around the Earth, which is also the origin of the Earth Centered Inertial coordinate frame, called {I}. A Local Vertical Local Horizontal coordinate frame, denoted with the letter {L}, is defined by locating its origin in a convenient orbit so that both the chaser and the target motion can be referred by means of relative distances from that as follows:

$$\mathbf{d}_B = \mathbf{r}_B - \mathbf{r}_L \tag{1}$$

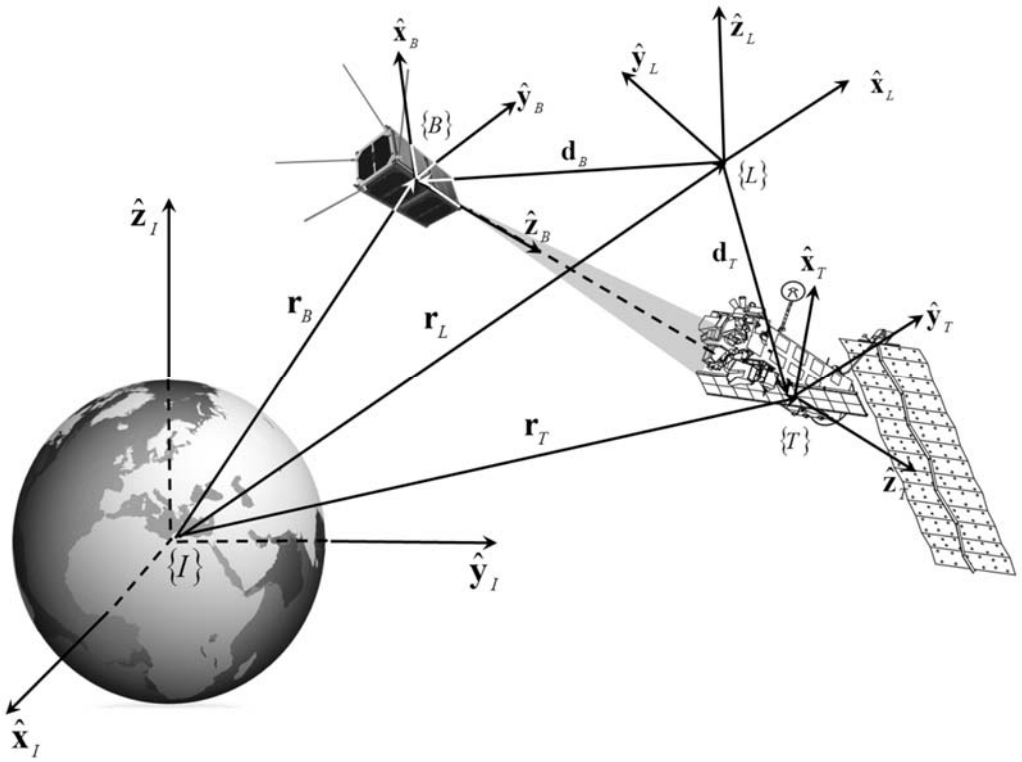

Figure 1. Schematic representation of the local vertical local horizontal {L}, of the chasing spacecraft {B} and of the target {T} coordinate frames

$$\mathbf{d}_T = \mathbf{r}_T - \mathbf{r}_L \tag{2}$$

The $\hat{\mathbf{x}}_L$ axis of the {L} coordinate frame is along the radial direction, the $\hat{\mathbf{z}}_L$ axis is directed as the normal to the orbital plane and the $\hat{\mathbf{y}}_L$ axis forms a right handed frame with the two other axes.

The main components and coordinate frames associated to the chaser spacecraft and the zooming camera are represented in Figure 2. Specifically, the frame {B} is rigidly attached to the spacecraft body and its origin is coincident with the center of mass G_B . The frame {C} is the camera frame and it is attached to the camera *c*. The 4 reactions wheels, denoted with *rw1, rw2, rw3* and *rw4*, are in a pyramidal configuration and their rotation axes are inclined with respect to the $\hat{\mathbf{x}}_B\hat{\mathbf{y}}_B$ body plane by an angle β. This configuration guarantees a 3 axis stabilization and reliability against the failures of one of the wheels [43]. The spacecraft main thruster is located along the $\hat{\mathbf{z}}_B$ body axis (th_{z+}) and it pushes along the +z direction. The other 5 small thrusters, namely th_{z-}, th_{x+}, th_{x-}, th_{y+} and th_{y-} allow for maneuvering along other directions.

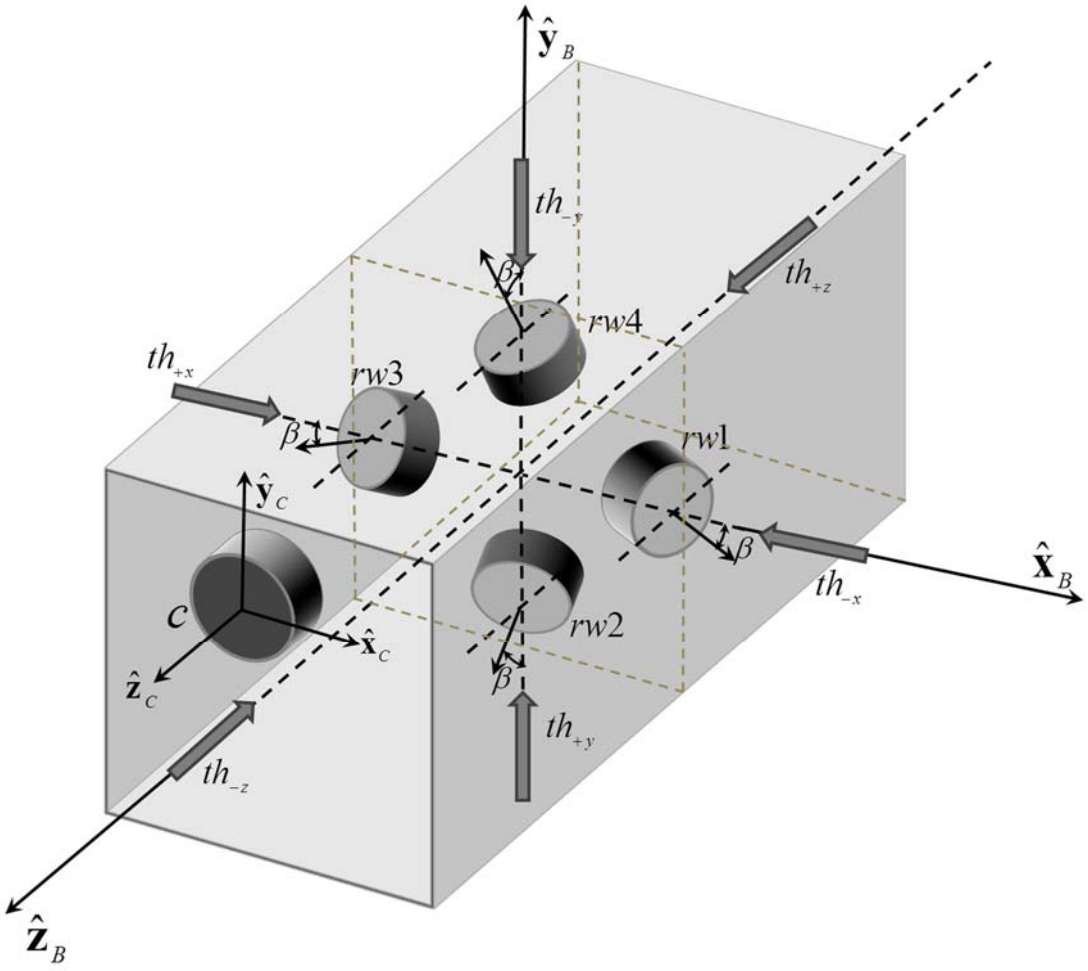

Figure 2. Schematic representation of the chaser the associated coordinate frames {B}, the camera frame {C}, the position and directions of the thrusters and of the reaction wheels.

In this study, it is assumed that the thrusters do not produce any torque to the spacecraft so that the attitude maneuvers are performed only by using the reactions wheels.

2.2 System dynamics

Both orbital and attitude dynamics are taken into account for describing the motion of the spacecraft. Concerning the orbital dynamics, it is convenient to refer to the position of both the chaser and target spacecraft with respect to the {L} reference frame, assuming that this frame is moving in a circular orbit. Thus, the relative dynamics of the chaser and target spacecraft are presented by the Clohessy-Wiltshire equations of motion [45]:

$$\begin{bmatrix} {}^{L}\dot{\mathbf{d}}_i \\ {}^{L}\dot{\mathbf{v}}_i \end{bmatrix} = \begin{bmatrix} \mathbf{A}_{11} & \mathbf{A}_{12} \\ \mathbf{A}_{21} & \mathbf{A}_{22} \end{bmatrix} \begin{bmatrix} {}^{L}\mathbf{d}_i \\ {}^{L}\mathbf{v}_i \end{bmatrix} + \begin{bmatrix} \mathbf{B}_1 \\ \mathbf{B}_2 \end{bmatrix} \mathbf{u}_{th} \tag{3}$$

where ${}^{L}\mathbf{d}_i = \begin{bmatrix} {}^{L}x_i & {}^{L}y_i & {}^{L}z_i \end{bmatrix}^T$ and ${}^{L}\mathbf{v}_i = \begin{bmatrix} {}^{L}\dot{x}_i & {}^{L}\dot{y}_i & {}^{L}\dot{z}_i \end{bmatrix}^T$ are the position and velocity vectors of the two spacecraft, where the right-subscript *i* can be substituted with T and B, as per target and chaser spacecraft, respectively. The left superscript *L* means that the components of the vectors are defined in the local horizontal local vertical reference frame. The matrices $\mathbf{A}_{11}$, $\mathbf{A}_{12}$, $\mathbf{A}_{21}$ and $\mathbf{A}_{22}$ are defined as follows:

$$\mathbf{A}_{11} = \begin{bmatrix} 0 & 0 & 0 \\ 0 & 0 & 0 \\ 0 & 0 & 0 \end{bmatrix} \quad \mathbf{A}_{12} = \begin{bmatrix} 1 & 0 & 0 \\ 0 & 1 & 0 \\ 0 & 0 & 1 \end{bmatrix}$$
$$\mathbf{A}_{21} = \begin{bmatrix} 3n_L^2 & 0 & 0 \\ 0 & 0 & 0 \\ 0 & 0 & -n_L^2 \end{bmatrix} \quad \mathbf{A}_{22} = \begin{bmatrix} 0 & 2n_L & 0 \\ -2n_L & 0 & 0 \\ 0 & 0 & 0 \end{bmatrix} \tag{4}$$

where $n_L = \sqrt{\mu_\oplus / r_L^3}$, $\mu_\oplus = 398600 km^3/s^2$ is the Earth's planetary constant, and r_L is the distance between the origins of the {L} and {I} coordinate frames. The control actions to the chaser are grouped in a vector $\mathbf{u}_{th} = [th_{+x} \quad th_{-x} \quad th_{+y} \quad th_{-y} \quad th_{+z} \quad th_{-z}]^T$, where each element can only be positive magnitude or zero (a thruster can only push the spacecraft.) The matrices $\mathbf{B}_1$ and $\mathbf{B}_2$ are defined as follows:

$$\mathbf{B}_1 = [\mathbf{0}]_{3\times 6}$$
$$\mathbf{B}_2 = \frac{1}{m_B} {}^{L}\mathbf{R}_i \; {}^{i}\mathbf{D}_{u_{th}} = \frac{1}{m_B} \begin{bmatrix} & {}^{L}\mathbf{R}_i & \end{bmatrix} \begin{bmatrix} 1 & -1 & 0 & 0 & 0 & 0 \\ 0 & 0 & 1 & -1 & 0 & 0 \\ 0 & 0 & 0 & 0 & 1 & -1 \end{bmatrix} \tag{5}$$

where m_B is the mass of the chaser, ${}^{i}\mathbf{D}_{u_{th}}$ distributes the thrust along specific directions with respect to the body coordinate frame, and ${}^{L}\mathbf{R}_i$ is the cosine direction matrix between the body coordinate frame and the local horizontal local vertical coordinate frame, defined as:

$$ {}^{L}\mathbf{R}_i = {}^{L}\mathbf{R}_I \; {}^{I}\mathbf{R}_i = {}^{L}\mathbf{R}_I \left({}^{i}\mathbf{R}_I \right)^{-1} \tag{6} $$

where ${}^{L}\mathbf{R}_I$ is the cosine direction matrix between the inertial and the local vertical local horizontal coordinate frames, and for the specific case under study it can be expressed by:

$$ {}^{L}\mathbf{R}_I = \begin{bmatrix} c_{\Omega_L} c_{\nu_L} - c_{i_L} s_{\Omega_L} s_{\nu_L} & s_{\Omega_L} c_{\nu_L} + c_{i_L} c_{\Omega_L} s_{\nu_L} & s_{i_L} s_{\nu_L} \\ -c_{\Omega_L} s_{\nu_L} - c_{i_L} s_{\Omega_L} c_{\nu_L} & -s_{\Omega_L} s_{\nu_L} + c_{i_L} c_{\Omega_L} c_{\nu_L} & s_{i_L} c_{\nu_L} \\ s_{i_L} s_{\Omega_L} & -s_{i_L} c_{\Omega_L} & c_{i_L} \end{bmatrix} \tag{7} $$

where Ω_L is the right ascension of the ascending node of the reference orbit, i_L is the inclination of the reference orbit, $\nu_L = \omega_L + \int_{t_0}^{t} n_L dt$ is the anomaly of the local reference frame, and ω_L is the argument of perigee of the reference orbit. In Eq.(7) the letters *s* and *c* represent the *sin* and the *cos* functions of the subscripted angle.

The rotation matrix ${}^{i}\mathbf{R}_I$ in Eq. (6) represents the spacecraft attitude with respect to inertial reference frame and can be expressed in terms of quaternions $\mathrm{Q}_i = [\mathrm{q}_i \quad \mathbf{q}_i]^T$ as follows ([46], pp.318-320):

$$ {}^{i}\mathbf{R}_I = \left[\left(\mathrm{q}_i^2 - \mathbf{q}_i^T \mathbf{q}_i \right) \mathbf{E} + 2\mathbf{q}_i \mathbf{q}_i^T - 2\mathrm{q}_i \tilde{\mathbf{q}}_i \right] \tag{8} $$

where $\mathbf{E}$ is the identity matrix and $\tilde{\mathbf{q}}_i$ is the skew-symmetric matrix of the vector part of the quaternion. The kinematic equations concerning the spacecraft attitude are expressed using quaternions form:

$$ \dot{\mathrm{Q}}_i = \frac{1}{2} \boldsymbol{\Omega}(\boldsymbol{\omega}_i) \mathrm{Q}_i = \frac{1}{2} \begin{bmatrix} \tilde{\boldsymbol{\omega}}_i & \boldsymbol{\omega}_i \\ -\boldsymbol{\omega}_i^T & 0 \end{bmatrix} \begin{bmatrix} \mathbf{q}_i \\ \mathrm{q}_i \end{bmatrix} \tag{9} $$

where $\boldsymbol{\omega}_i$ is the angular velocity of the spacecraft.

The attitude dynamics of the satellite can be modeled as follows ([47], pp. 107):

$$ \dot{\boldsymbol{\omega}}_i = -\mathbf{I}_i^{-1} (\boldsymbol{\omega}_i \times \mathbf{I}_i \boldsymbol{\omega}_i) - \mathbf{I}_i^{-1} (\boldsymbol{\omega}_i \times \boldsymbol{h}_w) + \mathbf{I}_i^{-1} \boldsymbol{T}_w + \mathbf{I}_i^{-1} \boldsymbol{T}_e \tag{10} $$

where $\mathbf{I}_i$ is the moment of inertia matrix of the spacecraft with respect to and expressed in the body frame, $\boldsymbol{h}_w$ is the angular momentum of the wheels, $\boldsymbol{T}_w$ is the torque provided by the reaction wheels acceleration and $\boldsymbol{T}_e$ is the external disturbing torque applied to the satellite, such as the gravity gradient torque, modeled by means of ([47], pp 109):

$$ \boldsymbol{T}_e = \frac{3\mu_{\oplus}}{r_i^3} \hat{\boldsymbol{r}} \times \mathbf{I}_i \hat{\boldsymbol{r}} \tag{11} $$

The torque provided by the reaction wheel increases the angular momentum of the wheels, and this effect is taken into account by means of the following equation:

$$\dot{\boldsymbol{h}}_w = -\boldsymbol{T}_w \tag{12}$$

Specifically, the torque $\boldsymbol{T}_{\mathrm{w}}$, provided by the reaction wheels in the configuration illustrated in Figure 2, is given by the following relation ([47],pp. 168-169):

$$\boldsymbol{T}_w = \boldsymbol{D}_{sw}\boldsymbol{U}_w = \begin{bmatrix} cos\beta & 0 & -cos\beta & 0 \\ 0 & cos\beta & 0 & -cos\beta \\ sin\beta & sin\beta & sin\beta & sin\beta \end{bmatrix} \begin{bmatrix} u_{w1} \\ u_{w2} \\ u_{w3} \\ u_{w4} \end{bmatrix} \tag{13}$$

where u_{w1}, u_{w2}, u_{w3} and u_{w4} are the control torque applied to each reaction wheel. An optimized algorithm for torque distribution among the wheels has been selected and applied to the model ([47], pp. 168-169] and [43]):

$$\boldsymbol{U}_w = \boldsymbol{D}_{sw}^T\left(\boldsymbol{D}_{sw}\boldsymbol{D}_{sw}^T\right)^{-1}\boldsymbol{T}_w \tag{14}$$

The mass consumption due to the thrusts is also modelled as follows:

$$\dot{m}_B = -\frac{1}{g_0}\left(\frac{th_{+x}}{I_{sp+x}} + \frac{th_{-x}}{I_{sp-x}} + \frac{th_{+y}}{I_{sp+y}} + \frac{th_{-y}}{I_{sp-y}} + \frac{th_{+z}}{I_{sp+z}} + \frac{th_{-z}}{I_{sp-z}}\right) \tag{15}$$

where $g_0 = 9.81 m/s^2$ and I_{sp+x} … I_{sp-z} are the specific impulses of the thrusters used as actuators.

The complete set of differential equations for the chaser spacecraft is represented by Eqs. (3), (9), (10), (12) and(15), while Eqs. (15) and (12) do not apply for the debris case, as its motion is uncontrolled. For the chaser dynamics, a reduced set of equations of motion will be considered for demonstrating the stability of the adopted visual servoing strategy. By considering the equations representing the dynamics of the system (i.e., the lower parts of Eq.(3) and Eq.(10)) and projecting them onto the camera coordinate frame, the following system of equations of motion can be obtained:

$$\boldsymbol{F}_B + \boldsymbol{F}_E = \boldsymbol{I}_c\ddot{\boldsymbol{x}}_c + \boldsymbol{C}_c \tag{16}$$

where $\ddot{\boldsymbol{x}}_c = [\dot{\boldsymbol{v}}_c^{\mathrm{T}} \quad \dot{\boldsymbol{\omega}}_c^{\mathrm{T}}]^{\mathrm{T}} \in \Re^6$ denotes the absolute linear and angular accelerations of the chaser satellite, $\boldsymbol{C}_c \in \Re^6$ contains the velocity/displacement-dependent non-linear terms of the chaser satellite, $\boldsymbol{F}_B \in \Re^6$ is the force and moment exerted by the satellite actuators, and $\boldsymbol{F}_E \in \Re^6$ contains the external/disturbing forces and torques applied to the chaser satellite.

2.3 Image-based visual servoing

From the images taken by the camera, a set of η non-coplanar image points of the target object can be extracted, and a vector of the visual features of the object can be defined as follows:

$$\boldsymbol{s} = \left[\boldsymbol{f}_1, \boldsymbol{f}_2, \ldots, \boldsymbol{f}_\eta\right]^{\mathrm{T}} \in \Re^{2\eta} \tag{17}$$

where each $\boldsymbol{f}_k$ contains the coordinates in the image plane of each selected image point:

$$\boldsymbol{f}_k = \left[f_{kx}, f_{ky}\right]^{\mathrm{T}} \in \Re^2 \tag{18}$$

where f_{kx} and f_{ky} are measured in pixels. The image-based visual servoing controller has to be designed in such a way that the guidance of the spacecraft is performed by tracking a desired trajectory in the image plane, $\boldsymbol{s}^*(t)$. As a result, the visual control generates the required linear and angular accelerations to be applied on the spacecraft for letting it perform a rendezvous with the observed object.

The relationship between velocities of the η extracted from the visual features in the camera image plane ($\dot{\boldsymbol{s}}_r \in \Re^{2\eta}$) and the angular and linear velocities of the camera ($\dot{\boldsymbol{x}}_{\mathrm{c}} \in \Re^6$) is described by the following equation:

$$\dot{\boldsymbol{s}}_r = \mathbf{L}_s \dot{\boldsymbol{x}}_{\mathrm{c}} \tag{19}$$

where $\mathbf{L}_s \in \Re^{2\eta \times 6}$ is the interaction matrix that relates the velocities of image feature points to the camera velocity vector [8]. This interaction matrix gathers all the interaction matrices related to each image feature in the image, as follows:

$$\mathbf{L}_s = \left[\mathbf{L}_{s1}^T \quad \mathbf{L}_{s2}^T \quad \ldots \quad \mathbf{L}_{s\eta}^T\right]^T \tag{20}$$

where each $\mathbf{L}_{sk}$ is the 2x6 interaction matrix of each image feature $k=1,2\ldots,\eta$.

The image acceleration or second derivative of $\boldsymbol{s}_{\mathrm{r}}$ is obtained by differentiating Equation (19) with respect to time, as follows:

$$\ddot{\boldsymbol{s}}_r = \mathbf{L}_s \ddot{\boldsymbol{x}}_{\mathrm{c}} + \dot{\mathbf{L}}_s \dot{\boldsymbol{x}}_{\mathrm{c}} \tag{21}$$

The goal of the image-based visual servoing controller is to track the desired trajectories of the selected η visual features in the image plane so that the following equation is satisfied:

$$(\ddot{\boldsymbol{s}}^* - \ddot{\boldsymbol{s}}) + \mathbf{K}_D(\dot{\boldsymbol{s}}^* - \dot{\boldsymbol{s}}) + \mathbf{K}_P(\boldsymbol{s}^* - \boldsymbol{s}) = 0 \tag{22}$$

where $\ddot{\boldsymbol{s}}^*$, $\dot{\boldsymbol{s}}^*$ and $\boldsymbol{s}^*$ are the desired accelerations, velocities and positions of the visual features in the image plane, respectively. $\mathbf{K}_P$ and $\mathbf{K}_D$ are proportional and derivative gain matrices, respectively. Thus, Equation (22) can be expressed in terms of image errors as follows:

$$\ddot{\boldsymbol{s}}^* + \mathbf{K}_D \dot{\boldsymbol{e}}_s + \mathbf{K}_P \boldsymbol{e}_s = \ddot{\boldsymbol{s}}_r \tag{23}$$

where $\boldsymbol{e}_s$ and $\dot{\boldsymbol{e}}_s$ are the image error and time derivative of the image error, respectively. Therefore, by inverting Equation (21) in order to obtain the desired spacecraft acceleration vector ($\ddot{\boldsymbol{x}}_{\mathrm{c}}$) from the reference image accelerations ($\ddot{\boldsymbol{s}}_r$), it is possible to obtain:

$$\ddot{\boldsymbol{x}}_c = \mathbf{L}_s^{+}\left(\ddot{\boldsymbol{s}}_r - \dot{\mathbf{L}}_s \dot{\boldsymbol{x}}_c\right) \tag{24}$$

where $\mathbf{L}_s^{+}$ is the Moore-Penrose pseudoinverse of $\mathbf{L}_s$, and $\ddot{\boldsymbol{s}}_r$ denotes the reference image accelerations of the visual features in the image plane.

Finally, by considering Equation (16) together with Equation (24), the following control law is obtained:

$$\boldsymbol{F}_B = \mathbf{I}_i \mathbf{L}_s^{+}\left(\ddot{\boldsymbol{s}}_r - \dot{\mathbf{L}}_s \dot{\boldsymbol{x}}_c\right) + \boldsymbol{C}_b - \boldsymbol{F}_E \tag{25}$$

leading to the closed-loop system represented by the following equation:

$$\mathbf{I}_i \ddot{\boldsymbol{x}}_c = \mathbf{I}_i \mathbf{L}_s^{+}\left(\ddot{\boldsymbol{s}}_r - \dot{\mathbf{L}}_s \dot{\boldsymbol{x}}_c\right) \tag{26}$$

that can be simplified by pre-multiplying by $\mathbf{L}_s\, \mathbf{I}_i^{-1}$, obtaining:

$$\mathbf{L}_s\, \ddot{\boldsymbol{x}}_c = \ddot{\boldsymbol{s}}_r - \dot{\mathbf{L}}_s \dot{\boldsymbol{x}}_c \tag{27}$$

Considering Equation (23) and using the relation given in Equation (21), Equation (27) can be rewritten as:

$$\ddot{\boldsymbol{e}}_s = -\boldsymbol{K}_D \dot{\boldsymbol{e}}_s - \boldsymbol{K}_P \boldsymbol{e}_s \tag{28}$$

showing that it leads to an asymptotic reduction of the image errors, and thus to the tracking of the desired image trajectories in the image plane. Therefore, the application of the proposed controller reduces to an asymptotically stable closed-loop system. It is also worth noting that the utilization of Equation (25) for tracking specific desired trajectories of visual features of the observed object will result in the computation of control actions to be applied to the chaser, in order for it to perform the desired rendezvous maneuvers with the observed target satellite.

3. Control in the invariant space

The aim of this paper is to modify the proposed image-based visual servoing controller to utilize camera zooming features. The camera can change the focal length when adaptive optics are used, resulting in changes in size of the observed objects in the camera image plane. A kinematic invariant controller is proposed in [44], performing the guidance independently of the changes in the camera intrinsic parameters. However, such velocity-based controller does not take into account the system dynamics that strongly characterize the problem of the space rendezvous. For this reason an image-based visual servoing controller that also includes dynamics of the chasing spacecraft is presented in this paper. Such controller generates the forces and moments to be applied to the spacecraft in order to track a given desired image trajectory in the invariant space. The invariant controller tries to minimize an error function that depends only on the relative position between the camera and the observed object, and it is completely independent from changes in camera intrinsic parameters. Therefore, a new

interaction matrix will be defined and used in the acceleration-based controller. This matrix relates the acceleration of the image features to the motion of the camera located at the spacecraft in the invariant space.

3.1 Invariant space

As it is already done for the classic image-based visual servoing control [33], a set of η non-coplanar image points can be obtained from the target object, $\boldsymbol{s} = \boldsymbol{f}_k$, $k \in 1 \dots \eta$. The image coordinates of a point $\boldsymbol{f}_k$, observed by a camera located in a $\boldsymbol{p}$ position, depends on the camera intrinsic parameters [41]. The same point observed by the camera at the desired position $\boldsymbol{p}^*$ is represented by another couple of image coordinates $\boldsymbol{f}_k^*$. The objective of the proposed visual controller is to guide the spacecraft using the extracted features $\boldsymbol{f}_k$ $k \in 1 \dots \eta$, in order to achieve the desired position of the camera $\boldsymbol{p}^*$ while tracking a given desired image trajectory. In order to make the spacecraft guidance independent from the camera intrinsic parameters, an error function is defined, which depends only on the camera position, and the projective transformation, proposed in [42], is used to obtain an invariant space with respect to those parameters.

Three non-collinear points are selected from the set of η non-coplanar image points observed by the camera. The corresponding image points in the current frame are $\boldsymbol{\varphi} = [\boldsymbol{f}_{h1}\ \boldsymbol{f}_{h2}\ \boldsymbol{f}_{h3}]$, where $\boldsymbol{f}_{hk} = [\boldsymbol{f}_{hkx}\ \boldsymbol{f}_{hky}\ 1]^{\mathrm{T}}$. The projection of the same points in the desired position are $\boldsymbol{\varphi}^* = [\boldsymbol{f}_{h1}^*\ \boldsymbol{f}_{h2}^*\ \boldsymbol{f}_{h3}^*]$. Both matrixes $\boldsymbol{\varphi}$ and $\boldsymbol{\varphi}^*$ are 3×3, and they will be used for defining two projective invariant spaces in the current and desired images, respectively. Image feature points $\boldsymbol{f}_{hk}$ and $\boldsymbol{f}_{hk}^*$ in the current and desired frames are converted to image features $\boldsymbol{\rho}_k$ and $\boldsymbol{\rho}_k^*$ in the invariant space by using the following transformations:

$$\begin{aligned} \boldsymbol{\rho}_k &= \boldsymbol{\varphi}^{-1}\boldsymbol{f}_{hk} \\ \boldsymbol{\rho}_k^* &= \boldsymbol{\varphi}^{-1}\boldsymbol{f}_{hk}^* \end{aligned} \tag{29}$$

The remaining η-3 points are instead used for defining the image error in the invariant space, as follows:

$$\boldsymbol{e}_q = \boldsymbol{s}_q - \boldsymbol{s}_q^*, \tag{30}$$

where $\boldsymbol{s}_q = [\boldsymbol{\rho}_4, \boldsymbol{\rho}_5, \dots, \boldsymbol{\rho}_\eta]$, of (3($\eta$-3)×1) size, includes the image features in the invariant space of the remaining points η-3.

3.2 Visual servoing in the invariant space

Through the definition of the invariant space and the corresponding error vector, it is now possible to adapt the image-based controller described in Section 2.3 in order to take into

account the changes in the focal length of the camera due to the zoom system. Indeed, Equation (19) can be expressed in the invariant space by using the projections defined in Equation (29), as follows:

$$\dot{\boldsymbol{s}}_q=\mathbf{L}_\rho\dot{\boldsymbol{x}}_\mathrm{c} \tag{31}$$

where the interaction matrix $\mathbf{L}_\rho$ is built from the interaction matrix of each invariant point, as follows:

$$\mathbf{L}_\rho=\left[\mathbf{L}_{\rho 4},\mathbf{L}_{\rho 5},\ldots,\mathbf{L}_{\rho n}\right]^T \tag{32}$$

For obtaining each of the $\mathbf{L}_{\rho k}$, *k=1…n*, which are included in Equation (32), it is necessary to differentiate Equation (29) as follows:

$$\dot{\boldsymbol{\rho}}_k=\frac{\partial\boldsymbol{\varphi}^{-1}}{\partial t}\boldsymbol{f}_{hk}+\boldsymbol{\varphi}^{-1}\dot{\boldsymbol{f}}_{hk}=\frac{\partial\boldsymbol{\varphi}^{-1}}{\partial t}\boldsymbol{\varphi}\boldsymbol{\rho}_k+\boldsymbol{\varphi}^{-1}\dot{\boldsymbol{f}}_{hk} \tag{33}$$

and use the following identity:

$$\frac{d\boldsymbol{\varphi}^{-1}}{dt}\boldsymbol{\varphi}=-\boldsymbol{\varphi}^{-1}\dot{\boldsymbol{\varphi}} \tag{34}$$

so that Equation (33) can be rewritten as:

$$\dot{\boldsymbol{\rho}}_k=-\boldsymbol{\varphi}^{-1}\dot{\boldsymbol{\varphi}}\boldsymbol{\rho}_k+\boldsymbol{\varphi}^{-1}\dot{\boldsymbol{f}}_{hk} \tag{35}$$

Equation (35) can then be expanded into:

$$\dot{\boldsymbol{\rho}}_k=\boldsymbol{\varphi}^{-1}\left(\dot{\boldsymbol{f}}_{hk}-\boldsymbol{\rho}_{1k}\dot{\boldsymbol{f}}_{h1}-\boldsymbol{\rho}_{2k}\dot{\boldsymbol{f}}_{h2}-\boldsymbol{\rho}_{3k}\dot{\boldsymbol{f}}_{h3}\right) \tag{36}$$

Thus, each $\mathbf{L}_{\rho k}$ can be expressed as follows:

$$\mathbf{L}_{\rho\mathrm{k}}=\boldsymbol{\varphi}^{-1}(\mathbf{L}_{s\mathrm{k}}-\boldsymbol{\rho}_{1k}\mathbf{L}_{s1}-\boldsymbol{\rho}_{2k}\mathbf{L}_{s2}-\boldsymbol{\rho}_{3k}\mathbf{L}_{s3}) \tag{37}$$

where $\mathbf{L}_{sk}$, $\mathbf{L}_{s1}$, $\mathbf{L}_{s2}$ and $\mathbf{L}_{s3}$ are the standard interaction matrices for image points *k, 1, 2* and *3*,respectively [33], with the addition of a third row of zeros.

Furthermore, Equation (24) has to be expressed in the invariant space as:

$$\ddot{\boldsymbol{x}}_\mathrm{c}=\mathbf{L}_\rho^{+}\left(\ddot{\boldsymbol{s}}_q-\dot{\mathbf{L}}_\rho\dot{\boldsymbol{x}}_c\right) \tag{38}$$

where it is necessary to calculate the value of $\dot{\mathbf{L}}_{\rho\mathrm{k}}$ for each invariant feature. An useful expression of each $\dot{\mathbf{L}}_{\rho\mathrm{k}}$ can be obtained by considering the time derivative of Equation (37) as follows:

$$\begin{aligned}\dot{\mathbf{L}}_{\rho\mathrm{k}}=&\frac{\partial\boldsymbol{\varphi}^{-1}}{\partial t}(\mathbf{L}_{sk}-\boldsymbol{\rho}_{1k}\mathbf{L}_{s1}-\boldsymbol{\rho}_{2k}\mathbf{L}_{s2}-\boldsymbol{\rho}_{3k}\mathbf{L}_{s3})\\&+\boldsymbol{\varphi}^{-1}\left(\dot{\mathbf{L}}_{sk}-\boldsymbol{\rho}_{1k}\dot{\mathbf{L}}_{s1}-\boldsymbol{\rho}_{2k}\dot{\mathbf{L}}_{s2}-\boldsymbol{\rho}_{3k}\dot{\mathbf{L}}_{s3}-\dot{\boldsymbol{\rho}}_{1k}\mathbf{L}_{s1}-\dot{\boldsymbol{\rho}}_{2k}\mathbf{L}_{s2}\right.\\&\left.-\dot{\boldsymbol{\rho}}_{3k}\mathbf{L}_{s3}\right)\end{aligned} \tag{39}$$

where $\dot{\mathbf{L}}_{sk}$ are the values of the time derivative of the classical interaction matrices for each of the feature points. Equation (39) contains the unknown term $\frac{\partial \boldsymbol{\varphi}^{-1}}{\partial t}$ whose expression can be found considering that:

$$\dot{\boldsymbol{f}}_{hk} = \mathbf{L}_{\mathrm{sk}} \dot{\boldsymbol{x}}_{\mathrm{c}} \tag{40}$$

$$\dot{\boldsymbol{f}}_{hk} = \boldsymbol{\varphi}\dot{\boldsymbol{\rho}}_k + \dot{\boldsymbol{\varphi}}\boldsymbol{\rho}_k \tag{41}$$

thus:

$$\mathbf{L}_{sk} = (\boldsymbol{\varphi}\dot{\boldsymbol{\rho}}_k + \dot{\boldsymbol{\varphi}}\boldsymbol{\rho}_k)\dot{\boldsymbol{x}}_c^{-1} \tag{42}$$

Therefore, Equation (39) can be rewritten by considering Equation (42):

$$\begin{aligned} \dot{\mathbf{L}}_{\rho\mathrm{k}} = {} & \frac{\partial \boldsymbol{\varphi}^{-1}}{\partial t}\left((\boldsymbol{\varphi}\dot{\boldsymbol{\rho}}_k + \dot{\boldsymbol{\varphi}}\boldsymbol{\rho}_k)\dot{\boldsymbol{x}}_c^{-1} - \dot{\boldsymbol{\varphi}}\boldsymbol{\rho}_k\dot{\boldsymbol{x}}_c^{-1}\right) \\ & + \boldsymbol{\varphi}^{-1}\left(\dot{\mathbf{L}}_{sk} - \boldsymbol{\rho}_{1k}\dot{\mathbf{L}}_{s1} - \boldsymbol{\rho}_{2k}\dot{\mathbf{L}}_{s2} - \boldsymbol{\rho}_{3k}\dot{\mathbf{L}}_{s3} - \dot{\boldsymbol{\rho}}_{1k}\mathbf{L}_{s1} - \dot{\boldsymbol{\rho}}_{2k}\mathbf{L}_{s2}\right. \\ & \left. - \dot{\boldsymbol{\rho}}_{3k}\mathbf{L}_{s3}\right) \end{aligned} \tag{43}$$

By using Equation (34) together with Equations (36) and (37), it is possible to obtain the following expression of $\dot{\mathbf{L}}_{\rho\mathrm{k}}$ that does not include the time derivative $\frac{\partial \boldsymbol{\varphi}^{-1}}{\partial t}$:

$$\begin{aligned} \dot{\mathbf{L}}_{\rho\mathrm{k}} = {} & \boldsymbol{\varphi}^{-1}(-\dot{\boldsymbol{\rho}}_{1k}\mathbf{L}_{s1} - \dot{\boldsymbol{\rho}}_{2k}\mathbf{L}_{s2} - \dot{\boldsymbol{\rho}}_{3k}\mathbf{L}_{s3}) \\ & + \boldsymbol{\varphi}^{-1}\left(\dot{\mathbf{L}}_{sk} - \boldsymbol{\rho}_{1k}\dot{\mathbf{L}}_{s1} - \boldsymbol{\rho}_{2k}\dot{\mathbf{L}}_{s2} - \boldsymbol{\rho}_{3k}\dot{\mathbf{L}}_{s3} - \dot{\boldsymbol{\rho}}_{1k}\mathbf{L}_{s1} - \dot{\boldsymbol{\rho}}_{2k}\mathbf{L}_{s2}\right. \\ & \left. - \dot{\boldsymbol{\rho}}_{3k}\mathbf{L}_{s3}\right) \end{aligned} \tag{44}$$

4 Simulation Results

A debris removal mission was simulated in order to verify the viability and analyze the performance of the proposed image-based direct visual servoing controller. A rendezvous maneuver with the Envisat satellite was identified as the goal of the mission. Envisat represents one of the targets that is being considered for the active debris removal by the European Space Agency, because of its mass, size and threat of collisions with other objects in orbit [49]. In order to safely remove such a massive object from its orbit, a system capturing process followed by a controlled reentry maneuver is necessary. It appears that an image based rendezvous maneuver is a necessary task for any mission aiming at the removal of such debris. In the following subsections a description of the parameters of the objects, actuators and sensors used in the simulations is provided, as well as the simulation results. Three different maneuvers are presented: a rendezvous to a tumbling object, a close approach maneuver and a far approach maneuver.

4.1 Simulation parameters

The mass properties and orbital parameters that characterize the target object under concern are reported in Table 2. The chaser is a satellite whose mass, sizes and inertia properties are reported in Table 1. The main characteristics of the onboard actuators and camera systems are reported in Table 3. The initial positions for the target and chaser spacecraft are $\boldsymbol{d_T} = [0.0 \quad 0.0 \quad 0.0]^T m$ and $\boldsymbol{d_B} = [0.0 \quad 20.0 \quad 0.0]^T m$, respectively. The quaternions representing the initial attitude of the target and chaser spacecraft are $\boldsymbol{Q_T} = [-0.2241 \quad -0.4830 \quad 0.1294 \quad 0.08365]^T$ and $\boldsymbol{Q_B} = [0.1830 \quad -0.500 \quad -0.500 \quad 0.6830]^T$, respectively.

Table 2 Mass, Size and Orbital Parameters of the Envisat Satellite

Mass (Kg)	Moments of Inertia (kg m^2)	Center of Mass (m)
$\boldsymbol{m_T = 7827.8}$	$\mathbf{I}_T = \begin{bmatrix} 17023.2 & 397.1 & -2171.4 \\ 397.1 & 124825.7 & 344.2 \\ -2171.4 & 344.2 & 129112.2 \end{bmatrix}$	$CoM_T = \begin{bmatrix} -3.9 \\ 0.0 \\ 0.0 \end{bmatrix}$
Length (m)	**Width (m)**	**Height (m)**
$\boldsymbol{l_T = 26.0}$	$\boldsymbol{w_T} = 10.0$	$\boldsymbol{h_T} = 26.0$
Semi-Major Axis (km)	**Eccentricity**	**RAAN (deg)**
$\boldsymbol{a_T = 7144.9}$	$e_T = 4.2e-4$	$\boldsymbol{\Omega_T} = 37.8$
Inclination (deg)	**Argument of Perigee (deg)**	**Initial True Anomaly (deg)**
$\boldsymbol{i_T = 98.4}$	$\boldsymbol{\omega_T} = 83.3$	$\boldsymbol{\nu_{0T}} = 0.0$

Table 1 Mass, Size and Orbital Parameters of the Chaser Satellite

Mass (Kg)	Moments of Inertia (kg m^2)	Center of Mass (m)
$\boldsymbol{m_B = 200.0}$	$\mathbf{I}_B = \begin{bmatrix} 230.4 & 0.0 & 0.0 \\ 0.0 & 259.2 & 0.0 \\ 0.0 & 0.0 & 288.0 \end{bmatrix}$	$CoM_B = \begin{bmatrix} 0.0 \\ 0.0 \\ 0.0 \end{bmatrix}$
Length (m)	**Width (m)**	**Height (m)**
$\boldsymbol{l_B = 2.6}$	$\boldsymbol{w_B} = 1.2$	$\boldsymbol{h_B} = 1.2$

Table 3 Onboard Camera and Reaction Wheels Properties (from [52])

Focal Length (mm)	Resolution (pix × pix)	Pixel Size (μm × μm)
8.0	1024×1024	10×10
Max Torque (Nm)	**Saturation Angular Momentum (Nms)**	**Wheel speed (rpm)**
0.2	$4.0 - 12.0$	6000

4.2 Results

4.2.1. Maneuver 1: Rendezvous to a tumbling target

The rendezvous to a tumbling target represents one of the most probable scenarios in both active debris removal missions. In order to perform a rendezvous maneuver towards this rotating target, the chasing spacecraft needs to synchronize its relative position and attitude motion so that the close approach might be performed in a safe way [12]. Such kind of synchronization is generally demanding in terms of fuel consumption and it can be performed only when the chaser is in proximity of the target debris. The image-based visual servoing approach presented in this paper results to be extremely useful in such cases. In fact once the visual features have been selected in the images seen from the camera, the controller calculate concurrently both attitude and position maneuvers in order to track them and consequently perform the rendezvous to the tumbling target.

Recent observations showed that Envisat is tumbling with an angular rate of approximately 1.5 deg/s [50] and this angular velocity has been set as initial angular velocity of the target in the following simulation. In Figure 3 the angular velocity of the tumbling target are represented. The chaser has to perform an approach to this moving target while synchronizing both its relative position and attitude with the debris tumbling motion. The resulting behavior of the system during the maneuver is illustrated by the sequence of images in Figure 4, where it is possible to notice that the chaser succeeds on pointing always towards the same face of the debris while this is randomly tumbling. The maneuver is performed after having identified the set of positions of the selected visual features of the target $\boldsymbol{s} = \left[\boldsymbol{f}_1 = (495, 549), \boldsymbol{f}_2 = (495, 469), \boldsymbol{f}_3 = (575, 469), \boldsymbol{f}_4 = (575, 549)\right]^T$ pix. and planned that such positions will

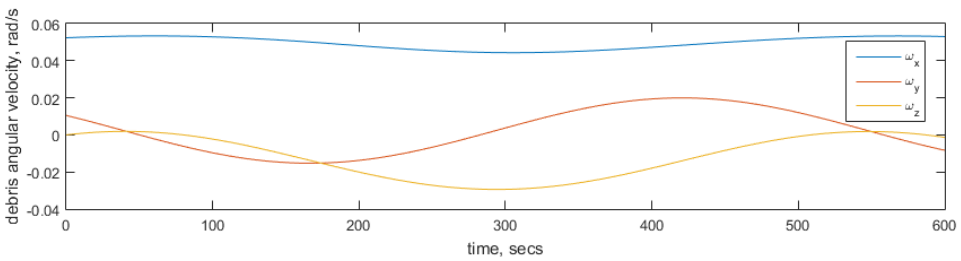

Figure 3. Debris angular velocity during the maneuver 1.

change linearly in the image plane so that at the end of the maneuver will reach $\boldsymbol{s}^* = [\boldsymbol{f}_1^* = (395, 649), \boldsymbol{f}_2^* = (395, 369), \boldsymbol{f}_3^* = (675, 369), \boldsymbol{f}_4^* = (675, 649)]^T$. The proportional and derivative gain matrices are $\mathbf{K}_P = 0.001\boldsymbol{E}$ and $\mathbf{K}_D = 0.08\boldsymbol{E}$, respectively.

The resulting behavior of the visual features in the image plane is represented in Figure 6. The resulting behavior shows that, due to the initial relative motion between chaser and target, the visual features tends to escape from the camera field of view. Thus, the computed control actions let these features being centered in the image plane and then a reduction of the distance between the two spacecraft is obtained by increasing the shape of the debris seen by the camera.

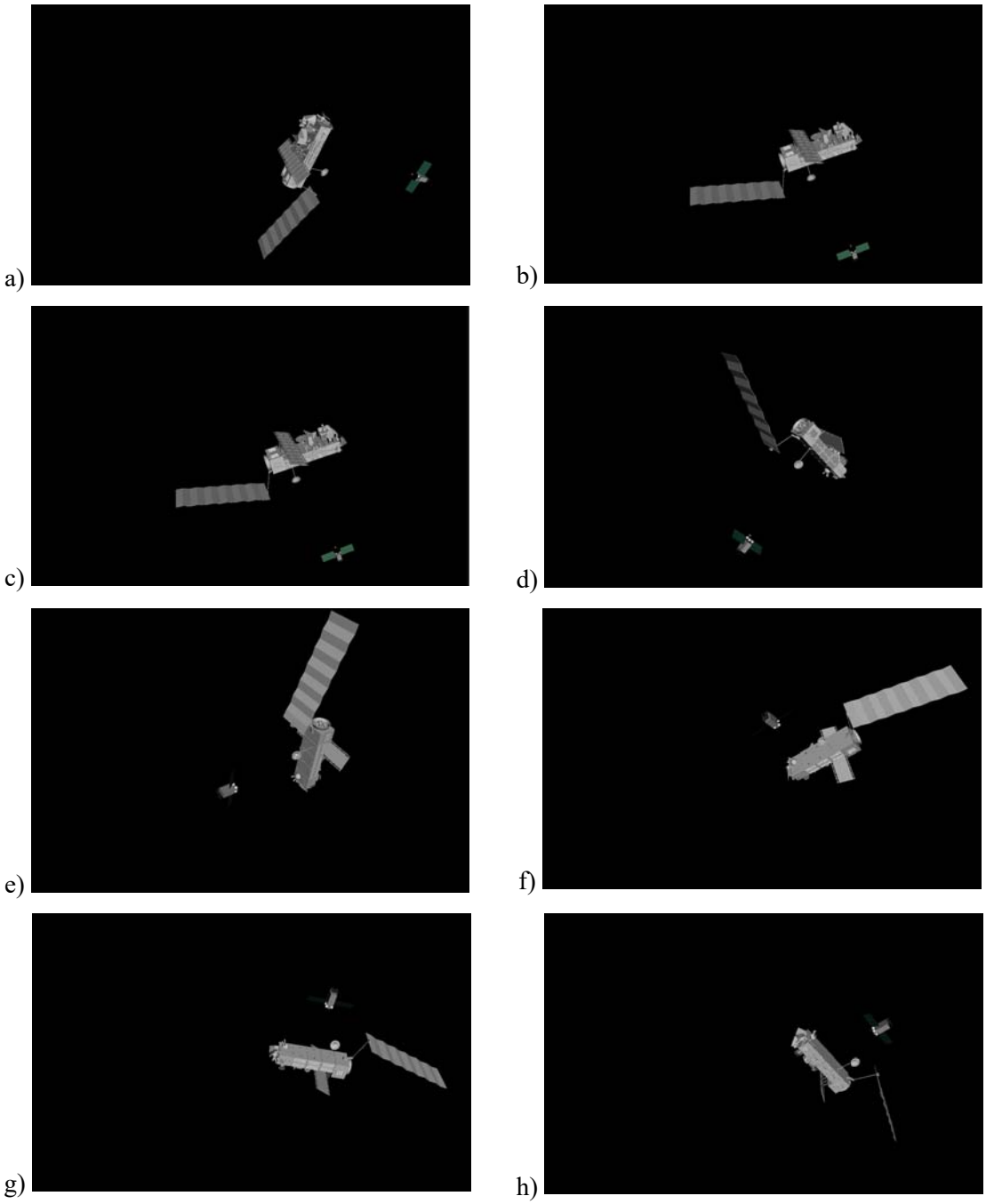

Figure 4. Behavior of the system during the maneuver 1.

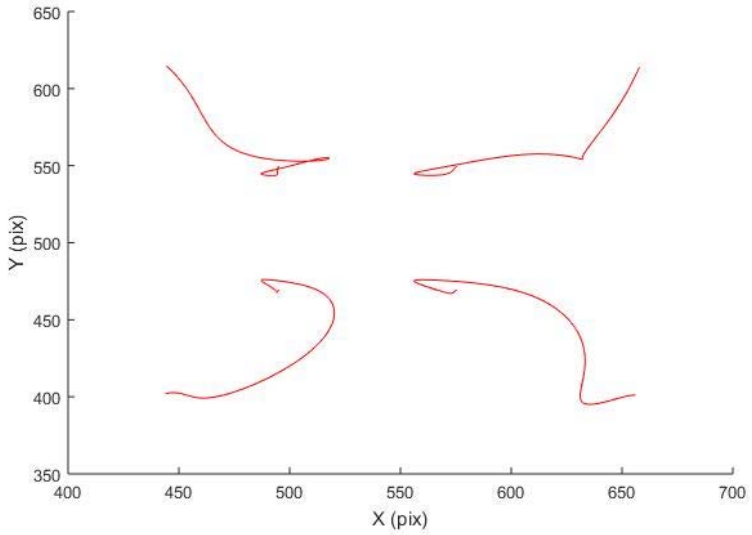

Figure 6. Trajectories of the visual features during the maneuver 1.

The thrusts calculated by the visual servoing controller during the maneuvers are shown in Figure 5. Initially the chasing spacecraft is subjected to a combined action of the thrusters along $\pm x$ directions so that the chaser can be acquire a synchronized revolution motion with respect to the target debris. The maximum thrust intensity required for performing this initial synchronization maneuver is less than 5N, which is within the typical operational range of this kind of actuators. The actions along the $\pm y$ direction are limited to a maximum value of 0.5N and allow the chaser to follow also the wobbling motion of the debris. The approach maneuver is realized through the action of the thrusters along $\pm z$ with a peak thrust of 1.3N for initially compensating both the gravity gradient and centrifugal actions, which tends to let the two bodies separate from each other, and then push the chaser to a closer position to the debris. The

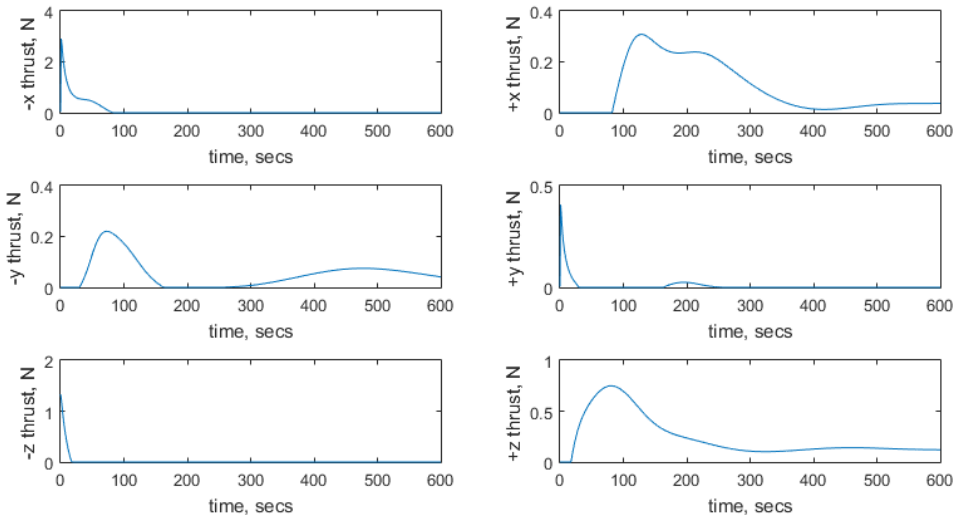

Figure 5. Thrust forces during the maneuver 1.

relative distance between the chasing spacecraft and the target object during the maneuver is shown in Figure 9. After an initial increase of the mutual distance, due to the combined action of the gravity gradient and centrifugal force, the chaser succeeds on performing the approach maneuver reducing the distance from 20m down to 8m.

The controller is also able to calculate the attitude corrections that allow the chaser always to point towards the same part of the debris. The torques applied to the reaction wheels of the chaser during the maneuver are represented in Figure 8. The attitude control system have to produce a greater torque at the begin of the maneuver, when the relative velocity between the

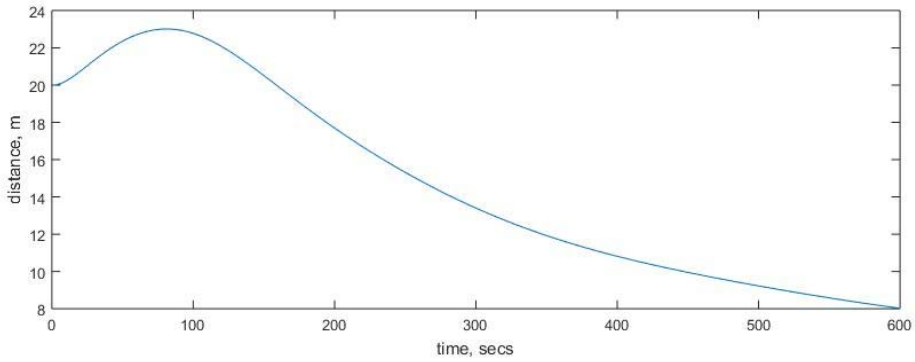

Figure 9. Relative distance between the chaser and the target during the maneuver 1.

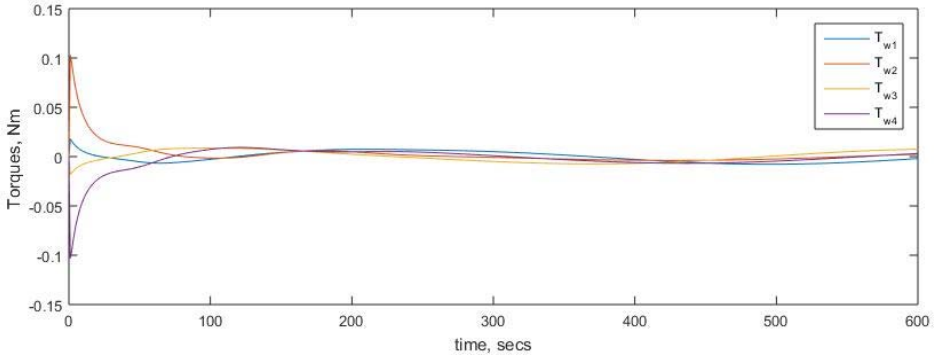

Figure 8. Torques applied to reaction wheels during maneuver 1.

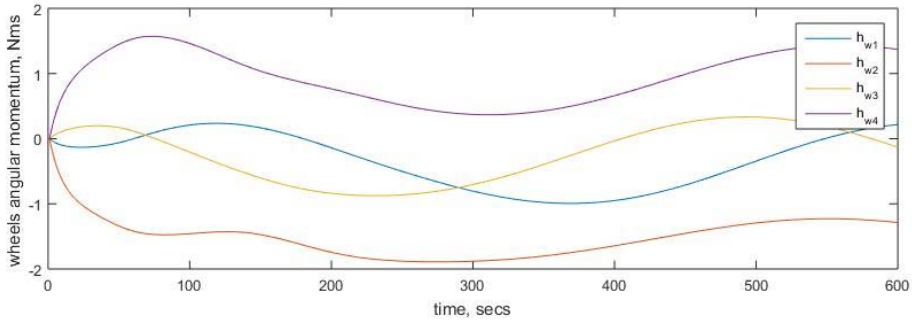

Figure 7. Angular momentum of reaction wheels during maneuver 1.

two objects is high. In any case the necessary torque does not exceed the 0.1Nm of magnitude, which is within the limit given in Table 3. Further, during this maneuver the angular momentum of the wheels does not exceed 2Nms (Figure 7), that is below the saturation limit of the wheels.

The relative angular velocity between the chaser and the target is illustrated in Figure 10. At the end of the maneuver the relative angular rates becomes stationary, meaning that the synchronization has been reached.

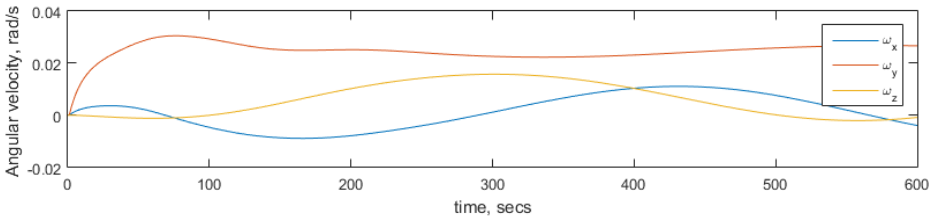

Figure 10. Relative angular velocity between the chaser and the target during maneuver

4.2.2. Maneuver 2: Close rendezvous by using zooming camera

The visual servoing technique, developed in Section 3.2 in the invariant space, allows for performing a rendezvous maneuver by employing a zooming camera. In fact, it is possible to define a desired trajectory in the invariant space, such that the onboard camera follows a straight line in the Cartesian space, as described in [48].

Figure 11 shows the initial and final position of the chaser and target spacecraft during a close rendezvous maneuver. At the beginning of the maneuver, the visual features are captured by using an initial focal length of 15mm. Then, a path $\boldsymbol{s}^*(t)$ is planned in the invariant space and tracked by the visual servoing controller in such way that the spacecraft follows a straight line in the 3D space. Simultaneously, the zoom is commanded to vary the focal length of the camera from 15 mm to 12 mm. The purpose of the zooming control is to extend the camera field of view when the target is moving out of the camera field of view, so that it is still possible to

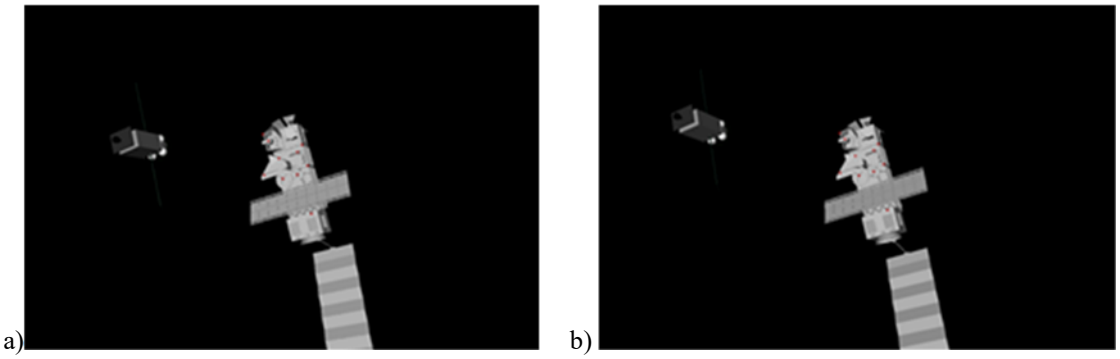

Figure 11. Obtained trajectory during the maneuver 4. a) Initial positions of the chasing and target spacecraft. b) Final positions of the chasing and target spacecraft.

perform the visual servoing maneuver with the same optical system even if the range between the objects is varying. The proportional and derivative gain matrices are $\mathbf{K}_P = 0.001\boldsymbol{E}$ and $\mathbf{K}_D = 0.05\boldsymbol{E}$, respectively.

The trajectories of the selected visual features during the rendezvous maneuver are shown in Figure 12 in red, while the same features of the target in their final desired position in the image plane, obtained by using the initial 15 mm focal length, are marked with symbol '*'. The error in the invariant space does not depend on the focal length of the camera system, and thus the chaser spacecraft accomplishes its maneuver, even if the trajectories of the features in the image plane do not reach their desired final positions. In fact, the focal length changes during the maneuver, and there is no correlation between the visual features in the image planes at the beginning and at the end of the maneuver. Indeed, despite this behavior of the visual features in the image plane, the error in the invariant space is maintained below an upper bound of 0.1 during the maneuver, as shown in Figure 13. The final desired relative configuration between the bodies is in any case reached at the end of the maneuver, as shown in Figure 14. To

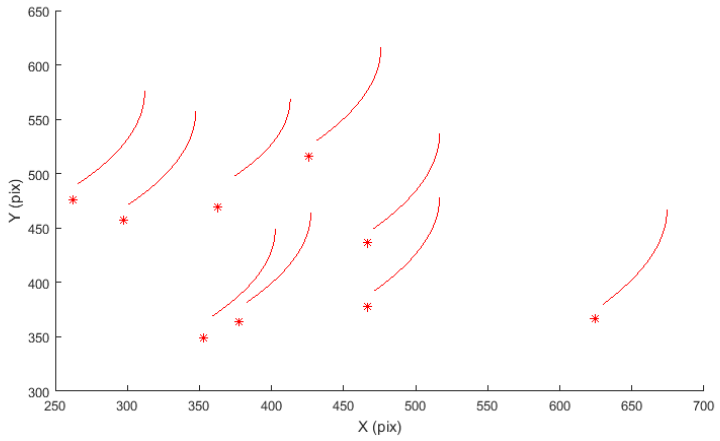

Figure 12. Image trajectory during the maneuver 2.

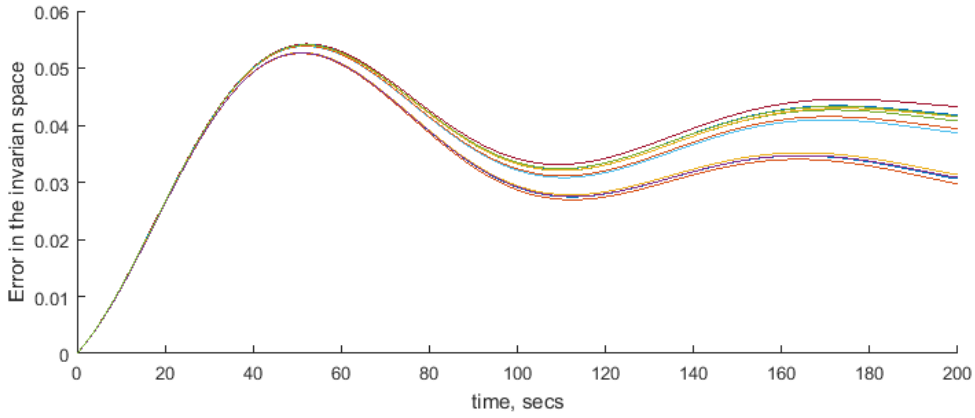

Figure 13. Error in the invariant space during the maneuver 2

complete the analysis, Figure 15 shows the computed thrusts to be applied during the maneuver.

4.2.3. Maneuver 3: Far rendezvous by using zooming camera

The advantages of using zooming cameras become evident when the range between the chaser and the debris changes significantly during the maneuver, and adjustments on the focal length are necessary to let the target not escape from the camera field of view. This is the case of the last simulation, where the target spacecraft is initially located 1km far from the chaser spacecraft. The initial and final views of the chasing spacecraft seen from the debris are shown

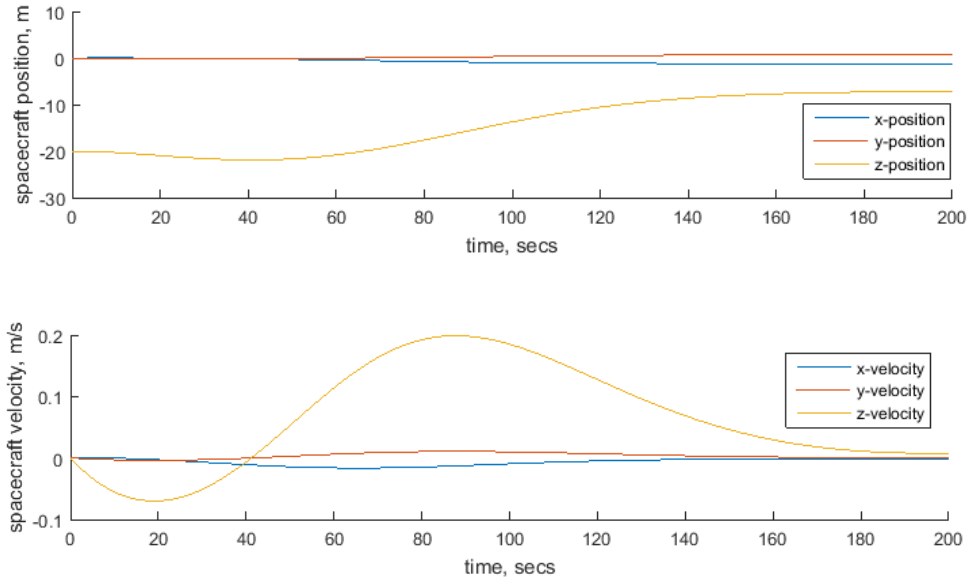

Figure 14. Position and velocity of the chaser satellite during the maneuver 2.

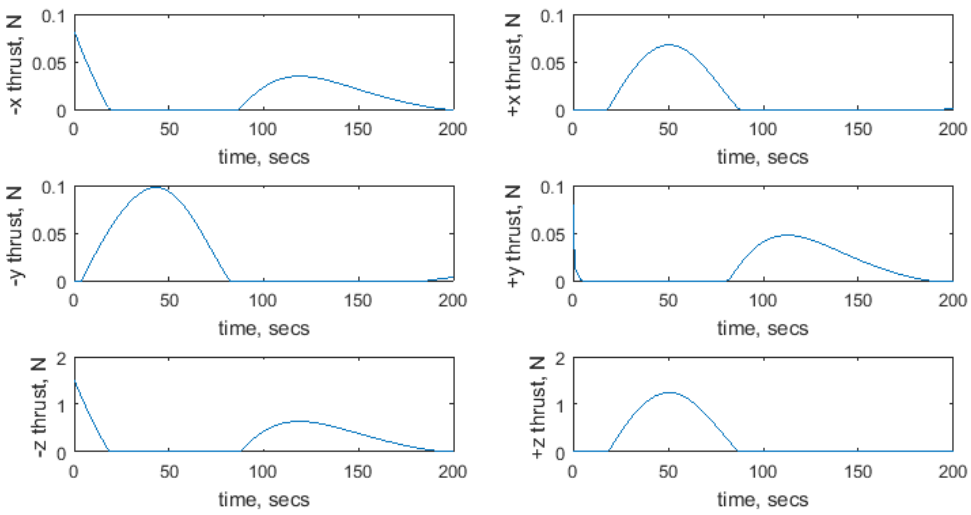

Figure 15. Thrust forces during maneuver 2.

in Figure 16. At the beginning of the maneuver, the chasing spacecraft has the dimension of a single pixel over a dark diffuse background in Figure 16.a, and its position is highlighted with a circle. On the other hand, all the main characteristics of the chaser are detectable from the target field of view at the end of the maneuver, as shown in Figure 16.b.

Similar to the previous maneuver, the desired trajectory is defined in the invariant space in such a way that the onboard camera follows a straight line between the initial and final desired distance between the spacecraft. The goal for this maneuver is the reduction from 1km to 20 m of chaser's distance from the debris. The camera focal length is initially set to 500 mm, and then progressively reduced during the maneuver down to 50 mm. The proportional and derivative gain matrices are $\mathbf{K}_P = 0.001\boldsymbol{E}$ and $\mathbf{K}_D = 0.05\boldsymbol{E}$, respectively. The desired visual features are learned by using the same camera parameters in Table 3, so that the final desired visual features of the debris, obtained with this set of parameters, are represented with '*' in Figure 17. However, as it was explained in the previous case, such desired visual features will not be reached by the trajectories traced in the image plane, because of the changes in the focal length during the zooming. In Figure 17 shows an initial oscillation along the vertical direction of all

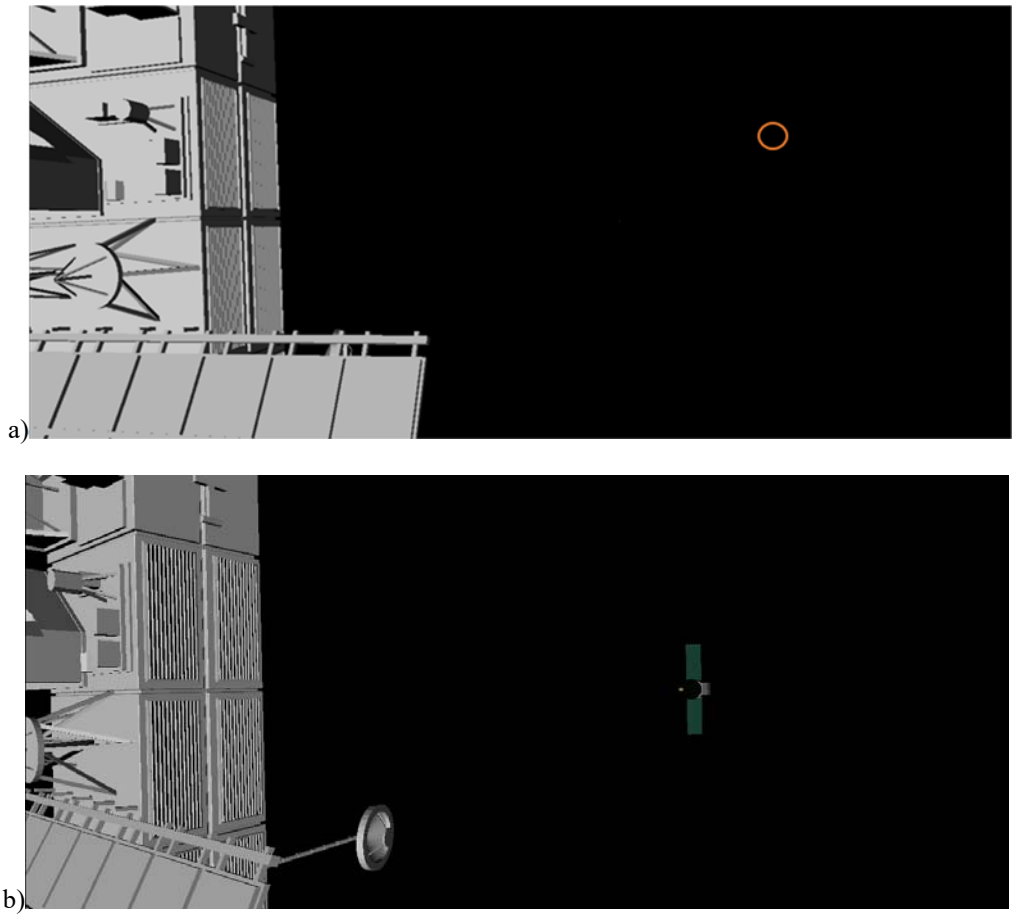

Figure 16. Obtained trajectory during the maneuver 3. a) Initial pose of the chasing and target spacecraft. b) Final pose of the chasing and target spacecraft.

the traces of visual features. This is essentially due to the initial adjustments performed by the chaser spacecraft for compensating the effects of the gravity gradient. Indeed, even if the changes in the lateral adjustments in position and velocity (along *x* and *y* directions) are small, as shown in the first 50 s of Figure 18 and Figure 19, the changes in the image plane are amplified because of the initial high value of the focal length. Figure 19 shows how, in this specific case, the main thrusts applied to the chaser are acting along its *z* axis, which is in fact the axis that is pointing toward the spacecraft. As a result, the range between the two bodies reduces to 15 min achieving the goal of this maneuver.

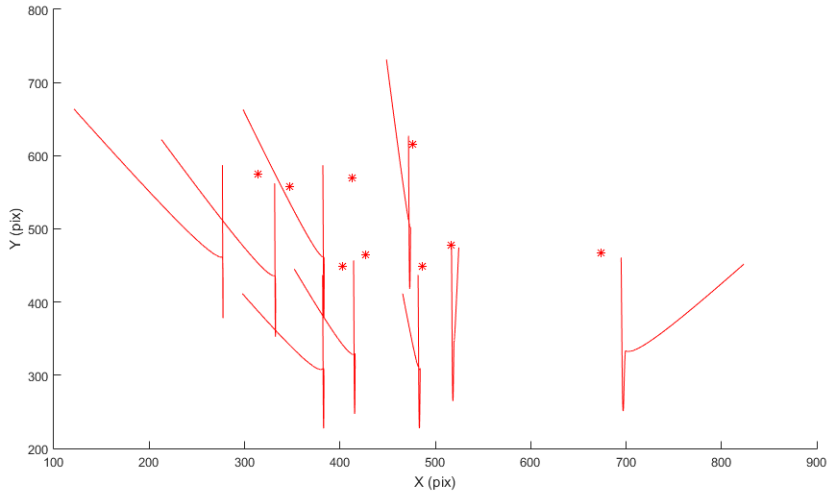

Figure 17. Image trajectory during the maneuver 3

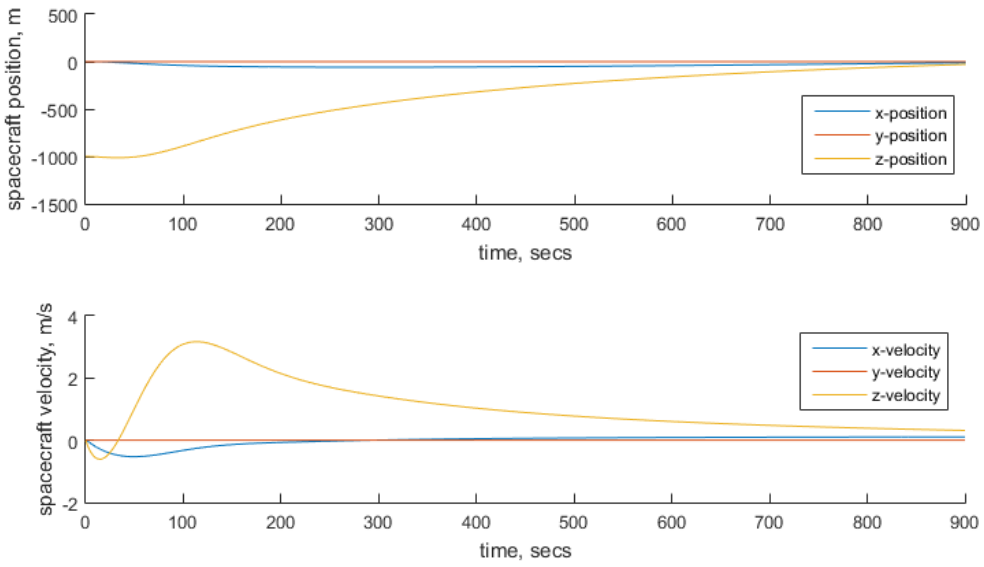

Figure 18. Position and velocity of the chaser satellite during the maneuver 3.

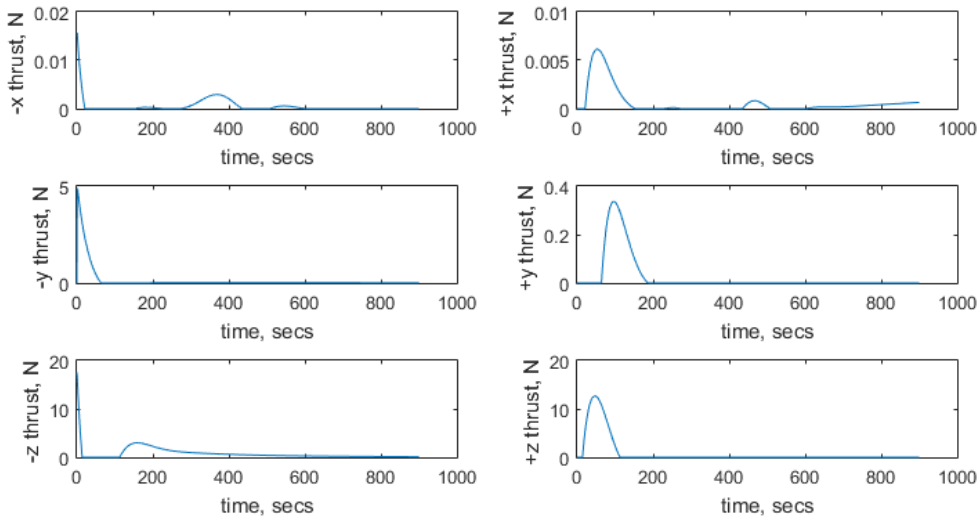

Figure 19. Thrust forces during the maneuver 3.

Table 4 Mass consumption during the maneuvers

Maneuver 1	Maneuver 2	Maneuver 3
$1.1 \cdot 10^{-1} kg$	$3.0 \cdot 10^{-3} kg$	$7.0 \cdot 10^{-1} kg$

4.2.4. Mass Consumption

All the maneuvers have also taken into account the mass reduction due to the ejection of the propellant from the onboard thrusters. The thrusters have been modelled by taking into account Hydrazine as the propellant ($I_{sp} = 200s$) and assuming that continuous thrust is allowed during the maneuvers [53]. The results are summarized in Table 4, where it is evident that the major mass consumption has been obtaned during the execution of the far approach (maneuver 3). Moreover, the approach and synchronization maneuver to a tumbling target (maneuver 1) requires an ammount of propellant comparable with the far approach case.

Finally, it worth noting that all the presented maneuver require a the propellant consumption that it is compatible with the standard mission configurations for active debris removal, showing that an image-based visual sevoing control can be proficiently applied in these kind of maneuvers.

5 Conclusions

A direct image-based controller that can be employed with zooming cameras has been presented and developed in this paper. The stability of the controller has been proved analytically, and its extension to the invariant space created by the zooming camera has also been verified through analytical developments. As a result, an adaptive and flexible tool has

been obtained, allowing for a concurrent control of both attitude and orbit of the chasing spacecraft during all phases of a non-cooperative rendezvous. The viability of the controller has been tested in a variety of test case maneuvers, including approaches to a tumbling object, as well as far and close rendezvous maneuvers. In all such cases the maneuvers have been accomplished, despite the perturbing actions due to the gravity gradient forces and torque. Moreover, it has also been shown that the utilization of the zooming camera allows for rendezvous maneuvers toward very far objects. This feature represents the main advantage over other already adopted control schemes for commanding rendezvous tasks. In fact, the zooming camera can overcome the technological limitations incurred in the previous missions, such as ATV and PRISMA, where two different camera systems were employed for performing far and close maneuvers. The numerical simulations demonstrated the viability of such control scheme by also taking into account realistic properties of the onboard zooming cameras as well as the reaction wheels and thrusters. The computed actuation efforts to be provided by the reaction wheels and of the necessary propellant mass show that such kind of maneuvers are feasible with the current state-of-the-art technology. Further investigations should address the problem of image-based optimal control concerning reaction wheels saturation as well as propellant consumption.

References

[1] Schaub, H., Jasper, L.E.Z., Anderson, P.V., McKnight, D. S., "Cost and risk assessment for spacecraft operation decisions caused by the space debris environment", *Acta Astronautica*, Vol. 113, Aug.–Sep. 2015, pp. 66-79.

[2] Flores-Abad, A., Ma, O., Pham, K., Ulrich, S., "A review of space robotics technologies for on-orbit servicing", *Progress in Aerospace Sciences*, Vol.68, 2014, pp. 1–26.

[3] IADC Space Debris Mitigation Guidelines, IADC-02-01 Rev. 1, Sep. 2007, www.iadc-online.org

[4] Flohrer, T., Schildknecht, T., Musci, R., "Proposed strategies for optical observations in a future European Space Surveillance network", *Advances in Space Research*, Vol. 41, No. 7, 2008, pp. 1010-1021.

[5] Donath, T., Schildknecht, T., Martinot, V., Del Monte, L., "Possible European systems for space situational awareness", *Acta Astronautica*, Vol. 66, No. 9–10, May–Jun. 2010, pp 1378-1387.

[6] Wang, T., "Analysis of Debris from the Collision of the Cosmos 2251 and the Iridium 33 Satellites," *Science & Global Security*, Vol.18, No. 2, 2010, pp. 87-118.

[7] Kessler, D.J., Cour-Palais, B.G., "Collision frequency of artificial satellites: the creation of a debris belt", *Journal of Geophysical Research*, Vol. 83, No. A6, 1978, pp. 2637-2646.

[8] Liou, J.C., Johnson, N.L., "Instability of the present LEO satellite populations", *Advances in Space Research*, Vol. 41, No. 7, 2008, pp. 1046-1053.

[9] Liou, J.C., "An active debris removal parametric study for LEO environment remediation", *Advances in Space Research*, Vol. 47, No. 11, 1 Jun. 2011, pp. 1865-1876.

[10] Shan, M., Guo, J., Gill, E., "Review and comparison of active space debris capturing and removal methods", *Progress in Aerospace Sciences*, Vol. 80, Jan. 2016, pp. 18-32.

[11] Graham, A.R., Kingston, J., "Assessment of the commercial viability of selected options for on-orbit servicing (OOS)", *Acta Astronautica*, Vol. 117, Dec. 2015, pp. 38-48.

[12] Felicetti, L., Gasbarri, P., Pisculli, A., Sabatini, M., Palmerini, G.B., “Design of robotic manipulators for orbit removal of spent launchers’ stages”, *Acta Astronautica*, Vol. 119, Feb.–Mar. 2016, pp. 118-130.
[13] Palmerini, G.B., Sabatini, M., Gasbarri, P., "Guidelines for active removal of non-functional targets designed to assist rendezvous and capture," *2016 IEEE Aerospace Conference*, Big Sky, MT, 2016, pp. 1-13.
[14] Alepuz, J.P., Emami, M.R., Pomares, J., “Direct image-based visual servoing of free-floating space manipulators”, *Aerospace Science and Technology*, Vol. 55, Aug. 2016, pp. 1-9.
[15] Pinard, D., Reynaud, S., Delpy, P., Strandmoe, S.E., “Accurate and autonomous navigation for the ATV”, *Aerospace Science and Technology*, Vol. 11, No. 6, 2007, pp. 490-498.
[16] De Rosa, D., Curti, F., "Visual Monitoring of Space Rendezvous: A Structure From Motion Problem", *AIAA/AAS Astrodynamics Specialist Conference and Exhibit*, Aug. 21-24, 2006, Keystone, Colorado
[17] Bodin, P., Noteborn, R., Larsson, R., Chasset, C., “System test results from the GNC experiments on the PRISMA in-orbit test bed”, *Acta Astronautica*, Vol. 68, No. 7–8, Apr–May 2011, pp. 862-872.
[18] Bodin, P., Noteborn, R., Larsson, R., Karlsson, T., D'Amico, S., Ardaens, J.S., Delpech, M., Berges. J.C, “The Prisma Formation Flying Demonstrator: Overview and Conclusions from the Nominal Mission". *Advances in the Astronautical Sciences*, Vol. 144, 2012, pp. 441-460.
[19] Bonnal, C., Ruault, J.M., Desjean, M.C., “Active debris removal: Recent progress and current trends”, *Acta Astronautica*, Vol. 85, Apr.–May 2013, pp. 51-60.
[20] Woffinden, D.C., Geller, D.K., "Observability Criteria for Angles-Only Navigation," *IEEE Transactions on Aerospace and Electronic Systems*, vol. 45, no. 3, pp. 1194-1208, Jul. 2009.
[21] Petit, A., Marchand, E., Kanani, K., “Vision-based space autonomous rendezvous: A case study”, *2011 IEEE/RSJ International Conference on Intelligent Robotic Systems*, 2011, pp. 619–624. doi:10.1109/IROS.2011.6094568.
[22] Gasbarri, P., Sabatini, M., Palmerini, G.B., “Ground tests for vision based determination and control of formation flying spacecraft trajectories”, *Acta Astronautica*, Vol. 102, Sep.–Oct. 2014, pp. 378-391.
[23] Song, L., Li, Z., Ma, X., “Autonomous rendezvous and docking of an unknown tumbling space target with a monocular camera”, *Proceedings of 2014 IEEE Chinese Guidance Navigation Control Conference*, 2014, pp. 1008–1013.
[24] Aghili, F., Kuryllo, M., Okouneva, G., English, C., "Fault-Tolerant Position/Attitude Estimation of Free-Floating Space Objects Using a Laser Range Sensor," *IEEE Sensors Journal*, vol. 11, no. 1, pp. 176-185, Jan. 2011.
[25] Woods, J.O., Christian, J.A., “Lidar-based relative navigation with respect to non-cooperative objects”, *Acta Astronautica*, Vol. 126, Sep.–Oct. 2016, pp. 298-311.
[26] Opromolla, R., Fasano, G., Rufino, G., Grassi, M., “Uncooperative pose estimation with a LIDAR-based system”, *Acta Astronautica*, Vol. 110, May–Jun 2015, pp. 287-297.
[27] Aghili, F., “A Prediction and Motion-Planning Scheme for Visually Guided Robotic Capturing of Free-Floating Tumbling Objects With Uncertain Dynamics”, *IEEE Transactions in Robotics,* Vol. 28, 2012, pp.634–649.
[28] Hafez, A.H.A., Anurag, V.V., Shah, S.V., Krishna, K.M., Jawahar, C.V., “Reactionless visual servoing of a dual-arm space robot”, *2014 IEEE International Conference Robotics and Automation*, pp. 4475–4480.
[29] Yu, F., He, Z., Qiao, B., Yu, X., “Stereo-Vision-Based Relative Pose Estimation for the Rendezvous and Docking of Noncooperative Satellites”, *Mathematical Problems in Engineering*, Vol. 2014, 2014, pp. 1–12.
[30] Kolb, F.M.; Kirschstein, S.; Krämer, D.; Würl, R., “Zoom Camera System for Space Applications”, *Proceedings of 11th Symposium on Advanced Space Technologies in Robotics and Automation*, ASTRA 2011, Apr. 12-14, 2011.

[31] Hull, A.B., Arsenault; R.H., Hulan, D.G., Morgan, W.F., "Design of a space-qualified zoom lens for the space station mobile servicing system video camera". *Proc. SPIE 2539, Zoom Lenses*, Vol. 37, Oct. 1995, doi:10.1117/12.222840
[32] Rienow, A., Graw, V., Heinemann, S., Schultz, J., Selg, F., Menz, G., "Earth observation from the ISS Columbus Laboratory – an open education approach to foster geographical competences of pupils in secondary schools", *Living Planet Symposium 2016*, Prague, Czech Republic; 2016 May 9-16
[33] Chaumette, F., Hutchinson, S., "Visual servo control. I. Basic approaches", *IEEE Robotics and Automation Magazine*, Vol. 13, 2006, pp. 82–90. doi:10.1109/MRA.2006.250573.
[34] Chaumette, F., Hutchinson, S., "Visual servo control. II. Advanced approaches [Tutorial]", *IEEE Robotics and Automation Magazine*, Vol. 14, 2007, pp. 109–118. doi:10.1109/MRA.2007.339609.
[35] Hutchinson, S.,.Hager, G.D., Corke, P. I., "A tutorial on visual servo control," *IEEE Transactions on Robotics and Automation*, Vol. 12, No. 5, pp. 651-670, Oct 1996, doi: 10.1109/70.538972
[36] Alabdo, A., Pérez, J., Garcia, G. J., Pomares, J., Torres, F., "FPGA-based architecture for direct visual control robotic systems", *Mechatronics*, Vol. 39, 2016, pp. 204-216.
[37] Benninghoff, H., Rems, F., Boge, T., "Development and hardware-in-the-loop test of a guidance, navigation and control system for on-orbit servicing", *Acta Astronautica*, Vol. 102, 2014, pp. 67-80, doi:10.1016/j.actaastro.2014.05.023.
[38] Hafez, A.H.A., Anurag, V.V., Shah, S.V., Krishna, K.M., Jawahar, C.V., "Reactionless visual servoing of a dual-arm space robot", *2014 IEEE International Conference in Robotics and Automation*, 2014: pp. 4475–4480. doi:10.1109/ICRA.2014.6907512.
[39] Ma, G., Jiang, Z., Li, H., Gao, J., Yu, Z., Chen, X., et al., "Hand-eye servo and impedance control for manipulator arm to capture target satellite safely", *Robotica*, Vol.33, 2015, pp. 848–864. doi:10.1017/S0263574714000587.
[40] Pérez, J., Emami, M. R., Pomares, J., "Direct image-based visual servoing of free-floating space manipulators", *Aerospace Science and Technology*, Vol 55, Aug 2016, pp. 1-9.
[41] Faugeras, O., Three-dimensional computer vision: a geometric viewpoint, MIT Press, Cambridge, MA, 1993.
[42] E. Malis, "Visual servoing invariant to changes in camera intrinsic parameters", *International Conference on Computer Vision*, Vancouver, Canada, Jul. 2001, Vol. 1, pp. 704-709.
[43] Hablani, H. B., "Sun-tracking commands and reaction wheel sizing with configuration optimization", *Journal of Guidance, Control, and Dynamics*, Vol. 17, No. 4, 1994, pp. 805-814.
[44] Xin, J., Chen, K., Bai, L., Liu, D., Zhang, J. "Depth Adaptive Zooming Visual Servoing For A Robot With A Zooming Camera", *International Journal of Advanced Robotic Systems*, 2013, Vol. 10, No.1, pp. 1 – 11.
[45] Alfriend, K. T, Vadali, S. R., Gurfil, P., How, J. P. and Breger, L., Spacecraft Formation Flying: Dynamics, Control and Navigation, Elsevier, Oxford, UK, 2010.
[46] Wie, B., 1998. Space Vehicle Dynamics and Control, AIAA Education Series
[47] Sidi, M.J., 1997. Spacecraft Dynamics and Control: a Practical Engineering Approach, Cambridge University Press
[48] Malis, E., "Visual servoing invariant to changes in camera intrinsic parameters", *IEEE Transaction on Robotics and Automation*, Vol. 20, No.1, pp.72-81, 2004.
[49] Gómez, N.O., Walker, S.J.I., "Earth's gravity gradient and eddy currents effects on the rotational dynamics of space debris objects: Envisat case study", *Advances in Space Research*, Vol. 56, No. 3, Aug. 2015, pp. 494-508, doi: 10.1016/j.asr.2014.12.031
[50] Sommer, S., Rosebrock, J., Cerutti-Maori, D., Leushacke, L., "Temporal analysis of Envisat's rotational motion", *Proc. 7th European Conference on Space Debris*, Darmstadt, Germany, 18–21 April 2017.
[51] www.cubesatshop.com
[52] Honeywell HR 0610 Reaction Wheel datasheet

[53] Airbus Space Systems Hydrazine Thrusters, http://www.space-propulsion.com/spacecraft-propulsion/hydrazine-thrusters/index.html